The Effect of the Corner Boundary Layer on Shock-induced Separation in a Rectangular Channel

Kshitij Sabnis* and Holger Babinsky†

Department of Engineering, University of Cambridge, Cambridge, CB2 1PZ, UK

Daniel S. Galbraith‡ and John A. Benek§

Air Force Research Laboratory, Wright-Patterson AFB, Ohio, United States

Wind tunnel experiments are conducted to investigate the effect of the corner regions of a Mach 2.5 channel flow on the response of the floor boundary layer to an oblique shock. To study this, two different nozzle setups are used, which produce distinct corner boundary layers for the same core flow and floor boundary layer. The setup with a higher-momentum corner flow exhibits milder corner separation. This, in turn, results in a central separation which is more two-dimensional and 18% shorter than for the setup with thicker corner boundary layers. The considerable difference in the flow structure between the two setups highlights the significant impact of the corner regions on shock-induced separation in supersonic channel flows, as well as the influence of nozzle geometry on this type of wind tunnel experiment.

I. Introduction

Corner boundary layers are often encountered in high-speed flows. For example, the intakes of supersonic aircraft, wing-body junctions, and turbine blade-hub junctions all contain streamwise corners, along which a boundary layer develops. However this geometry, which is often unavoidable, is also problematic. Since the corner region corresponds to the intersection of two viscous boundary layers, it contains very low momentum flow. When a shock wave impinges on the corner boundary layer, the adverse pressure gradient often causes separation. The corresponding stagnation pressure losses can have a significant detrimental effect. For instance, corner effects in the wing-body junction are estimated to contribute 4-6% of the total aircraft drag, while the inlet corner flows are believed to reduce the range of fighter aircraft by 9% [1].

In a channel flow, corner boundary-layer separation can have a substantial impact on the entire flowfield and cause significant departures from two-dimensionality even away from the sidewalls [2, 3, 4, 5]. The mechanism governing these effects is based on compression and expansion waves which are generated by the displacement effect of the corner separation, and which propagate away from the corners into the flow. These waves modify the streamwise adverse pressure gradient in other regions to inhibit, reduce or enhance separation there. These effects can be substantial – for example, recent experiments on an oblique shock boundary-layer interaction in a Mach 2.5 channel flow showed that the streamwise extent of the central separation varied by a factor of five as the location of corner separation point was shifted [5, 6].

The separation of the corner boundary layer is therefore important in determining the separation characteristics of the entire flowfield. However, there are still no consistently successful techniques to mitigate corner separation, apart from (possibly) targeted surface bleed [7, 8]. The difficulties in tackling this issue can arguably be directly attributed to our lack of understanding of the complicated flow physics in streamwise corners, and of their interactions with shock waves. Furthermore, corner separation cannot be reliably predicted by computational codes typically used in industry. This is due, in part, to a notable lack of high-quality reference data to validate numerical simulations.

*PhD Student, Department of Engineering, University of Cambridge.

†Professor in Aerodynamics, Department of Engineering, University of Cambridge, AIAA Associate Fellow.

‡Engineer, Computational Sciences Centre, AFRL Aerospace Systems Directorate.

§Director, Computational Sciences Centre, AFRL Aerospace Systems Directorate, AIAA Fellow.

A key factor influencing this separation is the momentum within the corner boundary layer – this is affected by the thickness of the constituent floor and sidewall boundary layers as well as the structure of streamwise vortices which exist in this region [9, 10, 11]. These vortices, generated by the anisotropy in Reynolds stresses, serve to transfer momentum between the core flow and the boundary layers, thus increasing the momentum within the corner region.

In order to better predict separation, it is necessary to obtain deeper physical insight into how the momentum within the corner flow influences shock-induced separation. This paper examines the separated flowfield for two quite different corner boundary layers in a channel flow featuring an oblique shock reflection. In order to isolate the effects of the corner region itself, the tests are conducted in the same facility and at identical conditions (Mach 2.5, 8° flow deflection).

The generation of two different corner boundary layers for otherwise unchanged tunnel flow makes use of recent work, which has shown that the nozzle geometry in supersonic wind tunnels strongly influences the corner flows [12]. The pressure distribution in the nozzle induces a secondary flow within the sidewall boundary layers. This flow affects the sidewall boundary-layer thickness as well as the structure of the corner vortices, two key parameters in determining the structure of the corner boundary layer. Therefore, the use of two different nozzle setups enables the generation of quite distinct corner flows without affecting other flow conditions.

The experimental study presented in this paper focuses measurements on the separation behaviour of the floor boundary layer, for two tunnel configurations with different corner flows but otherwise equivalent conditions. The considerable differences in separated flow field between the two setups are explained in the context of known mechanisms, related to the waves generated by the displacement effect of the corner separation. These differences highlight the importance of the corner regions on separation in supersonic channel flows, as well as the significance of nozzle geometry in wind tunnel experiments of this kind.

II. Experimental Method

A. Wind tunnel setup

Experiments are performed in Supersonic Wind Tunnel No. 1 at the Cambridge University Engineering Department. This is a blow-down wind tunnel, driven by a high-pressure reservoir. The facility is capable

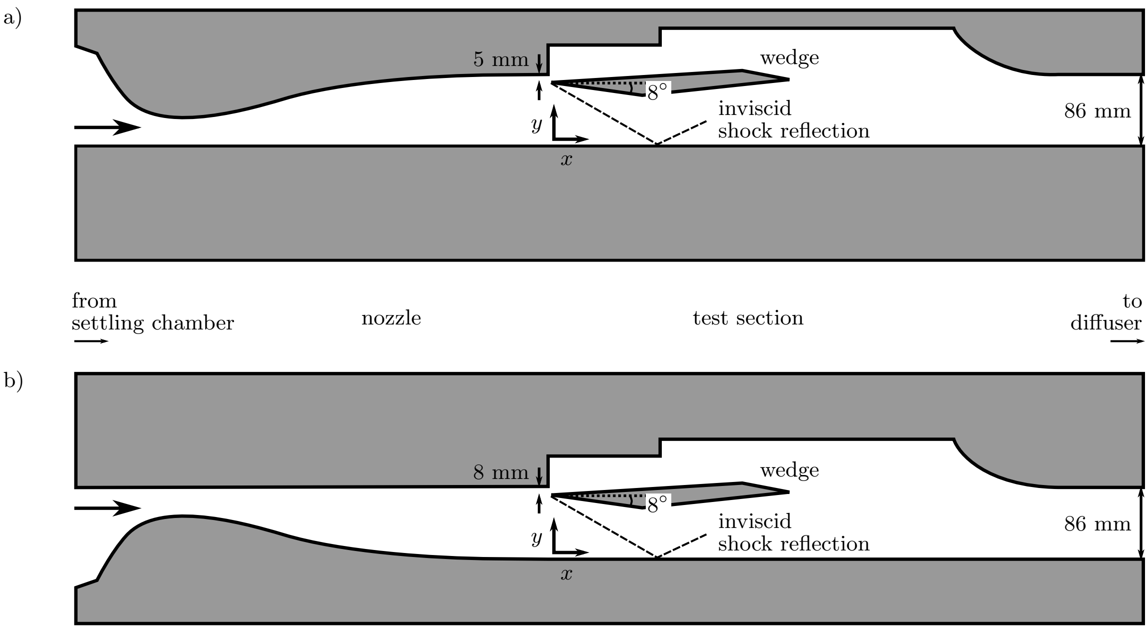

Figure 1. Tunnel arranged in the two configurations used in this study, a) setup A and b) setup B. The test section width is 114 mm.

of operating at Mach numbers between 0.7 and 3.5, depending on the installed nozzle configuration; for this study, the nominal freestream Mach number is fixed at $M_\infty = 2.5$. The stagnation pressure is set to 380 ± 1 kPa and the operating stagnation temperature is measured as 285 ± 5 K; this corresponds to a unit Reynolds number of approximately 40×10^6 m^{-1}.

The setup in the test section is shown in figure 1. An asymmetric, or "half", two-dimensional nozzle configuration is used; this consists of one contoured and one flat surface. In order to produce different corner flows in the bottom tunnel corners, two different types of nozzle setup (denoted A and B) are used; these are described in section III.

A full-span wedge on the tunnel ceiling produces a flow deflection angle of 8°, and thus generates an oblique shock. In order to prevent tunnel unstart, the wedge is retracted during startup and is then deployed once supersonic flow has been established. The wedge is placed below the upper surface of the tunnel; this enables the ceiling boundary layer to disappear into the gap and ensures that the shock is generated in clean flow. The difference in gap size between the two setups is explained in section III.

The oblique shock wave then impinges on the turbulent, naturally-grown boundary layer on the tunnel floor. This is approximately 6 mm thick, and has a Reynolds number based on incompressible displacement thickness of around $\mathrm{Re}_{\delta_i^*} = 24{,}000$.

The rectangular test section of the tunnel has a width of 114 mm and a height of 86 mm. The coordinate system convention is shown in figure 1. x represents the streamwise direction, as measured from the end of the nozzle; y indicates the floor-normal direction, with $y = 0$ mm set at the tunnel floor; z is the spanwise coordinate measured from the centre span, such that $z = \pm 57$ mm correspond to the tunnel sidewalls.

B. Measurement techniques

Several techniques are used in combination to probe the flowfield. A z-type schlieren system with a horizontal knife-edge enables visualisation of density gradients and allows spanwise-averaged flow features to be identified.

The topology of the separated flowfield is surveyed by using the time-averaged skin-friction lines from surface oil-flow visualisation. This technique involves coating the tunnel floor with an oil made from paraffin, finely-powdered titanium dioxide, oleic acid and lubricating oil. This is an intrusive method and there is a small error due to oil-flow producing an inaccurate indication of separation location (by about 0.2 boundary-layer thicknesses = 1.2 mm) [13]. Nevertheless, oil-flow visualisation allows the flow topology to be determined, and comparisons of the size of separation regions between different setups are considered to be reliable.

Steady-state surface pressure measurements are conducted using pressure-sensitive paint (PSP). The surface of interest is sprayed with a special polymer binder seeded with luminescent molecules. When irradiated by UV light, the resultant luminescence intensity ratio $(\frac{I_{\mathrm{ref}}}{I(p,T)})$ is dependent on the local pressure, as specified by the Stern-Volmer relation [14]:

$$\frac{I_{\mathrm{ref}}}{I(p,T)} = A(T) + B(T)\frac{p}{p_{\mathrm{ref}}}$$

The luminescence is measured using a Nikon D7000 camera, and the reference condition is taken with the wind tunnel off ($p_{\mathrm{ref}} = 101$ kPa everywhere). The pressure in the separated flowfield varies from 29-57 kPa; this range of pressures is sufficiently large to provide reliable measurements [15]. In order to determine the values of $A(T)$ and $B(T)$ in the Stern-Volmer relation, in-situ calibration is performed using five 0.3 mm diameter static pressure taps connected to a differential pressure transducer (error: $\pm 1\%$) [16]. This calibration enables absolute pressure values on the target surface to be extracted from the measured light intensity. A comparison between static tap pressures and the calibrated PSP data places an error bound of 3% on these measurements. However, in regions where the thermal properties change (e.g. filler material or attachment screws) or where reflections from the tunnel walls distort the measured luminescence, the calibration is no longer valid and a much greater error is observed.

The streamwise and floor-normal flow velocities, u and v respectively, are measured by two-component laser Doppler velocimetry (LDV). The flow is seeded with paraffin in the settling chamber; previous measurements of particle lag through a normal shock have placed the seeding droplet diameter in the range 200-500 nm. The measured velocities have an error of 1% and 14% for u and v respectively; there are contributions from the number density of seeding particles and from the laser optics. Boundary-layer traverses are carried out with resolution $\Delta y \approx 0.1$ mm. The ellipsoidal probe volume spans 0.1 mm in the streamwise direction and 2 mm in the spanwise direction.

The measured boundary-layer data is fitted to theoretical profiles (figure 2). A Sun & Childs (1973) fit [17], adapted to include a van Driest compressibility correction, is used for the outer layer; this combines a log-law of the wall region with a Coles wake function. The viscous sublayer is modelled using a Musker (1979) fit [18]. These fitted profiles are then used to calculate characteristic boundary-layer integral parameters. This avoids errors caused by poor measurement resolution near the wall and therefore provides a more accurate estimate of integral boundary-layer parameters. The boundary-layer properties are determined in their incompressible forms, as these are less sensitive to variations in Mach number and require fewer assumptions to calculate from raw velocity data. The LDV data obtained in this study typically has around 40 measurement points within the boundary layer and the closest data point to the wall is at around $y^+ = 80$. This corresponds to an uncertainty in integral parameters of around 5% for an equilibrium turbulent boundary layer [19].

III. Creation of two different corner boundary layers

This study examines the influence of the corner regions on the behaviour of the flowfield with an oblique shock reflection. It is therefore necessary to generate two different corner boundary layers in the same facility without affecting other flow parameters, such as the core Mach number or the floor boundary-layer thickness. The significant influence of the nozzle geometry on the corner boundary layers in supersonic wind tunnels

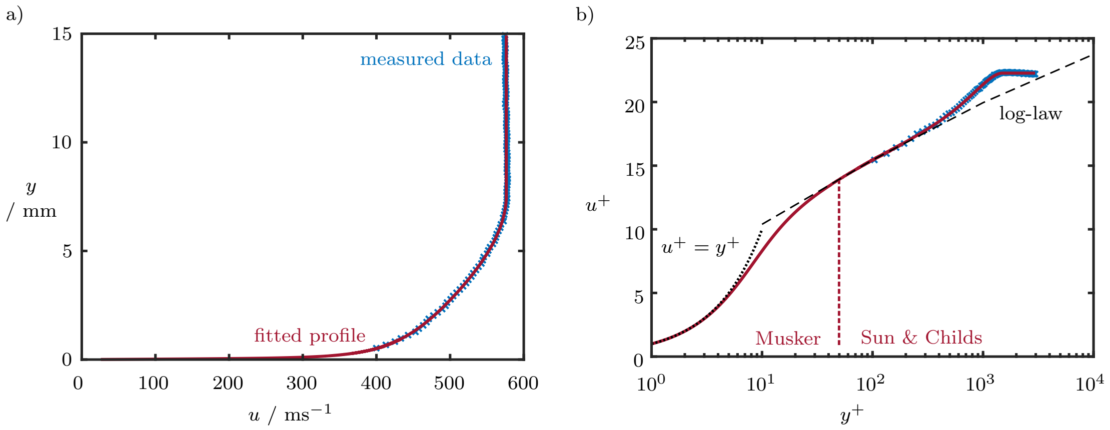

Figure 2. Boundary-layer LDV data and fitted profile in a) dimensional, and b) non-dimensional units. Measurements performed at $x = 60$ mm, $z = 0$ mm. In b), the data are presented in non-dimensional wall units, $u^+ = \frac{u}{u_\tau}$ and $y^+ = \frac{y u_\tau}{\nu_w}$. The error bars are contained within the symbol size with $\Delta u = 5$ ms^{-1} and $\Delta y = 0.1$ mm

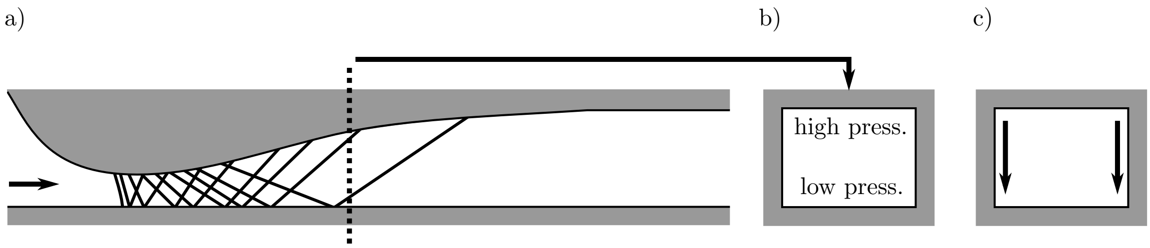

Figure 3. Schematic of the hypothesised secondary flows for the half nozzle setup: a) inviscid expansion wave pattern through the nozzle; b) the cross-sectional pressure distribution upstream of the nozzle exit; c) induced secondary flows in sidewall boundary layers.

allows this to be achieved [12].

As depicted in figure 1, a two-dimensional half nozzle configuration is used for this purpose. The two distinct corner flows are produced by installing the half nozzle such that the contoured surface is either on the ceiling (setup A) or the floor (setup B).

Figures 3a and 3b show how the expansion wave pattern within the nozzle leads to a vertical pressure gradient. The sidewall boundary layers contain low-momentum flow which is most susceptible to this pressure gradient, and so a secondary flow is set up (figure 3c). For this nozzle type, the secondary flow consists of vertical velocities within the sidewall boundary layer, which are directed away from the contoured surface and towards the flat surface. The secondary flow transports fluid within the sidewall boundary layers, and thus the boundary-layer thickness grows from the ceiling to the floor (figure 4). These effects, in turn, have a profound impact on the flow in the corner regions of the test section.

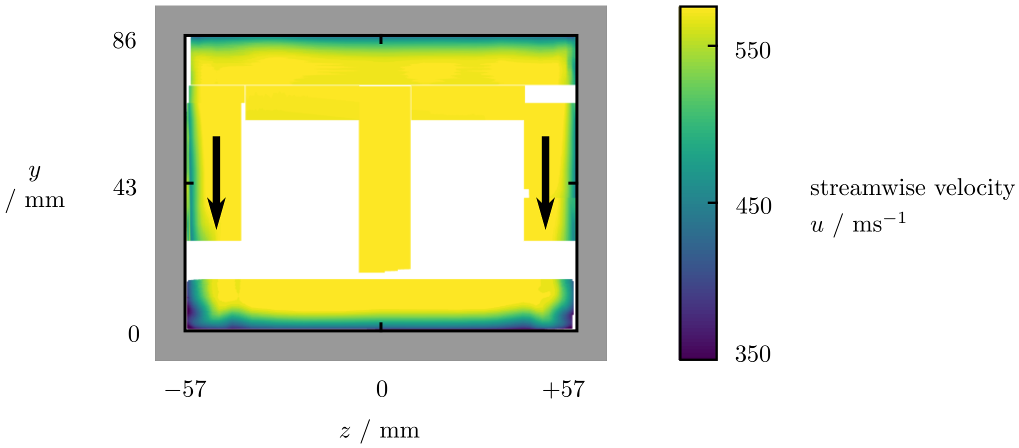

Figure 4. LDV measurements of the streamwise velocity across the tunnel cross-section, measured at $x = 120$ mm. The direction of sidewall secondary flows are identified by solid arrows.

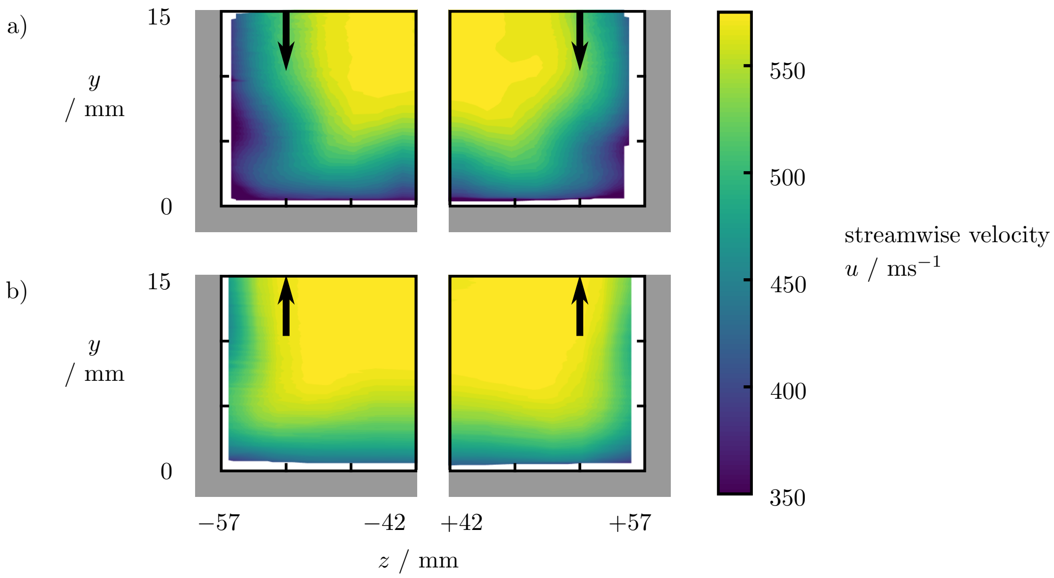

Figure 5. The streamwise velocity (u) in 15×15 mm regions around the bottom tunnel corners for a) setup A and b) setup B. These are measured at $x = 120$ mm. The direction of sidewall secondary flows are identified by solid arrows.

a) i. ii.

b) c)

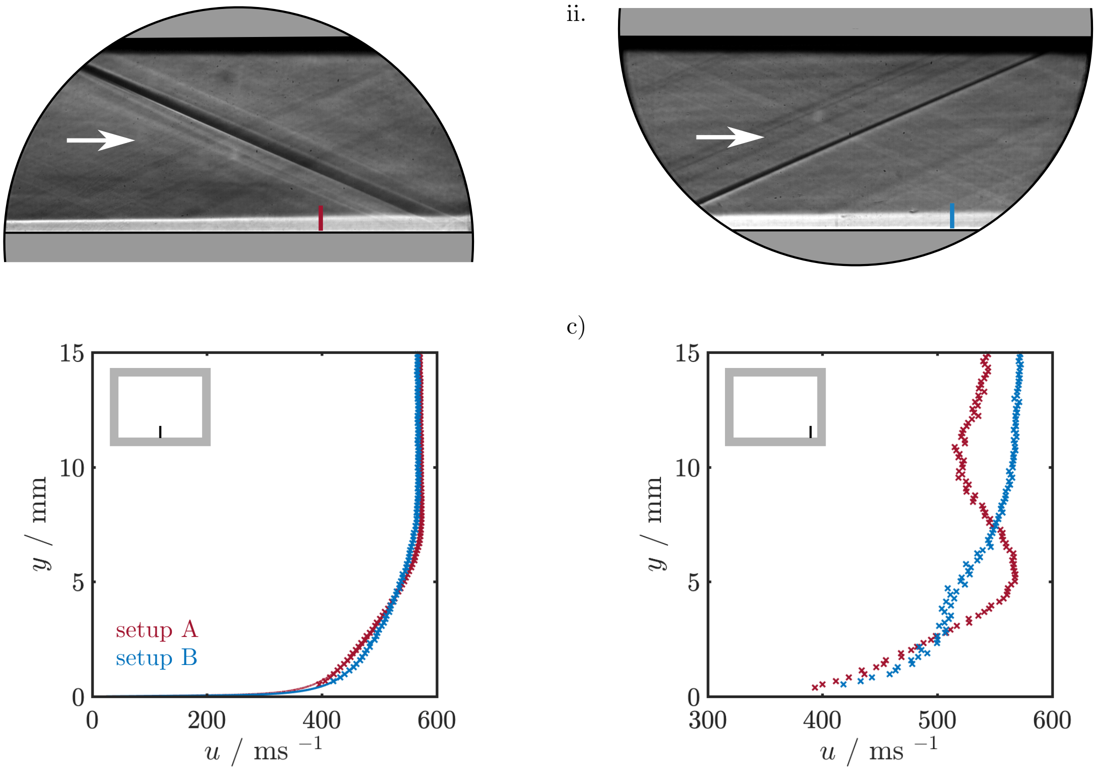

Figure 6. a) Schlieren images with the empty tunnel for i. setup A and ii. setup B. Comparison of boundary-layer profiles, measured using LDV at $x = 120$ mm a) on the tunnel centre span, and b) at $z = 52$ mm.

Measurements of the bottom corner boundary layers produced by the two setups are presented in figure 5. The floor boundary layers in the two types of corner flow appear to have roughly the same thickness. However, the sidewall boundary layers in setup A are thicker than those from setup B. As a result, the corners of setup A have flow with significantly lower momentum than the equivalent regions in setup B.

Schlieren images of the flow in the empty wind tunnel are shown figure 6a for setups A and B. A prominent wave, originating from a junction between constituent liner blocks, is visible in both setups. However, static pressure measurements have shown this wave to be weak in strength, with the Mach number over the entire working section deviating by just 0.03 from a mean value of 2.48 [12]. The floor boundary layers (integrated in the spanwise direction) are also visible in the schlieren images. These suggest (in agreement with figures 4 and 5) that the floor boundary layers in both setups have approximately the same thickness, an important requirement for this study.

The equivalence of the floor boundary layers can be more quantitatively compared by considering the floor boundary-layer profiles on the tunnel centre span measured using LDV (figure 6b). The measured profiles are similar but not identical. The corresponding fitted parameters, tabulated in 1 show that the boundary-layer displacement thickness and shape factor differ by 13% and 5% respectively. Corresponding profiles within the corner boundary layer (at $z = 52$ mm) are shown in figure 6c. The non-equilibrium nature of the boundary layer here means that it is not possible to obtain integral parameters through profile fitting. However, it is clear that while the differences between setups A and B are non-negligible for the centre-span floor boundary layer, they are significantly smaller than those measured in the corner regions.

Therefore, whilst it is important to consider these differences in incoming floor boundary layer during interpretation of the separated flowfield, it may be reasonable to attribute differences between the two setups primarily to the corner boundary layers.

Note: Position of wedge The difference in placement of the shock-generating wedge between the two setups is due to the sidewall secondary flows detailed in figures 3. In setup A, the wedge is placed 5 mm

Setup	δ / mm	δ_i^* / mm	θ_i / mm	H_i
A	7.7	1.00	0.75	1.33
B	8.7	0.87	0.69	1.27

Table 1. Incompressible floor boundary-layer parameters, measured at $x = 120$ mm and $z = 0$ mm, for experimental profiles presented in figure 6b.

beneath the tunnel's upper surface, so that the ceiling boundary layer disappears into the gap. However, the ceiling in setup B corresponds to the flat surface, with thicker sidewall and corner boundary layers. This means that the leading edge of a wedge 5 mm below the ceiling would still be in these boundary layers across much of the tunnel span. Therefore, the wedge is dropped by a further 3 mm, to leave an 8 mm gap into which the boundary layer can disappear; the shock is then generated in clean core flow.

The different wedge position has one main effect – the shock in setup B impinges on the floor boundary layer approximately 6 mm (*i.e.* about one boundary-layer thickness) upstream of that in setup A. To account for this difference an alternative coordinate system is used, where $\tilde{x}$ is the streamwise coordinate relative to the inviscid shock-reflection location. In other words, $\tilde{x} = x - 140$ mm for setup A and $\tilde{x} = x - 135$ mm for setup B. This enables direct comparison of equivalent locations with respect to the inviscid interaction.

IV. Results & Discussion

Setup A

Figure 7 shows a schlieren image of the response of the floor boundary layer to the incident oblique shock for setup A. The wedge is visible at the top of the image. The flow deflection caused by the leading edge and the bottom corner of the wedge generate an oblique shock and an expansion fan (denoted "wedge expansion") respectively. The wedge expansion complicates the flowfield, so we restrict our attention to the features upstream of the first expansion wave.

The wave pattern is representative of a typical separated oblique shock–boundary-layer interaction (SBLI). The incident shock causes the incoming floor boundary layer to separate. The flow deflection at the upstream edge of the separation produces a separation shock, the curvature of the separation bubble causes a series of expansion waves, and the turning of the flow as it reattaches results in a reattachment shock.

A streamwise LDV traverse 15 mm from the tunnel floor is shown in figure 8. The streamwise velocity u shows a profile in accordance with the waves captured in the figure 7. The velocity drops as it passes through the incident shock and deflects by $8.2 \pm 1.1°$. These error bounds encompass the flow deflection angle of 8°

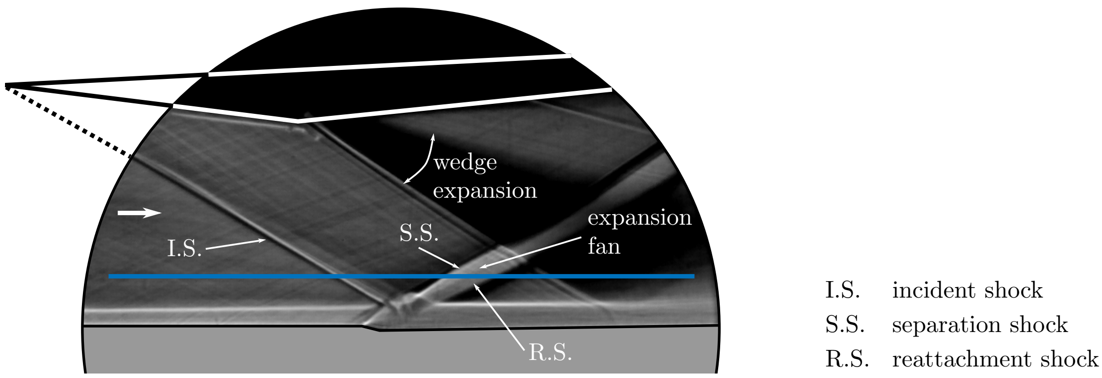

Figure 7. Schlieren image of the oblique shock–boundary-layer interaction for setup A. The blue line denotes the LDV traverse location for figure 8.

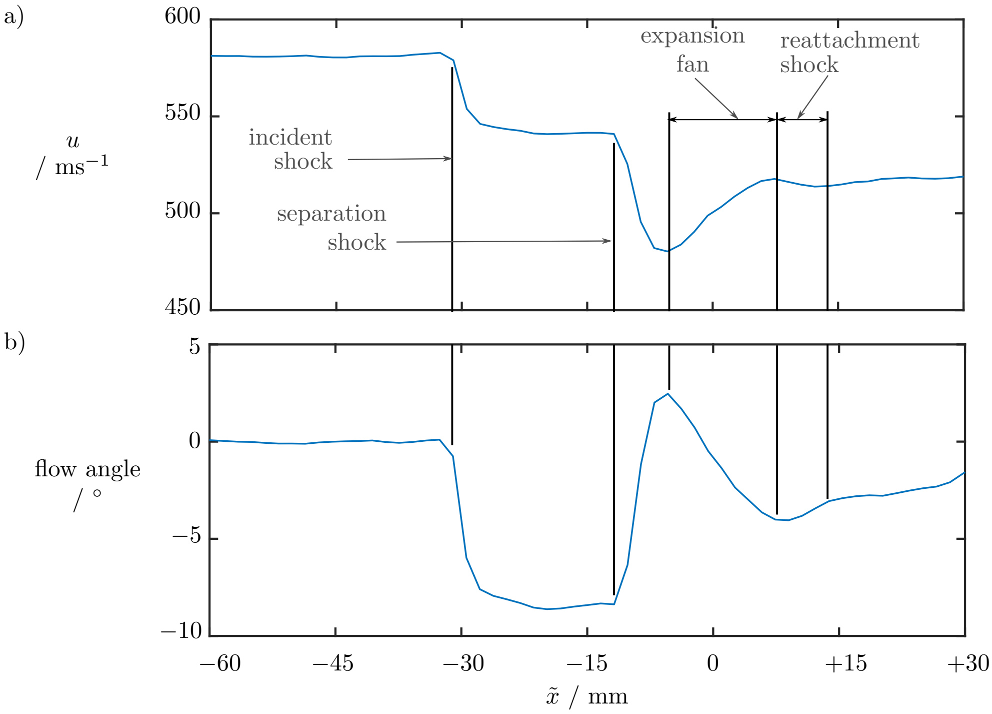

Figure 8. Streamwise LDV traverse at $y = 15$ mm and $z = 0$ mm, for setup A. The figure shows a) streamwise velocity u, and b) the local flow angle, measured upwards from horizontal.

set by the wedge. The following two deceleration regions bounding an area of re-acceleration correspond to the separation shock and reattachment shock respectively. The reattachment shock appears to be weak in strength and smeared, even outside the boundary layer. Note that even prior to the wedge expansion, the flow has not returned to horizontal, but still has a downawards deflection angle of 2°. There is, however, a gradual turning of the flow towards horizontal, perhaps associated with weak waves generated due to the displacement effect as the boundary layer recovers.

Figure 9 shows the surface oil-flow visualisation on the tunnel floor. The separated regions are highlighted in the figure – these have been identified from a close study of the skin friction line topology using the methods detailed in reference 5. There is significant separation on the centre span, which is relatively two-dimensional. This central separation extends 25.2 mm in the streamwise direction and covers 68% of the tunnel span. Separated by a narrow channel of attached flow are regions of corner separation on each side. These begin 31.1 mm and 29.8 mm further upstream than the central separation and cover 15.2% and 15.7% of the tunnel span, in the negative-z and positive-z corners, respectively. These measures of the separated flow field agree extremely well with those obtained from previous similar experiments [5].

The steady-state surface pressure distribution, measured using PSP, is presented in figure 10a. Note that, due to reflections from the sidewall, pressure readings at the top of the image exceed their true values. Upstream of the interaction, there is a uniform low pressure region. Across the SBLI, there is a rapid pressure rise. This is two-dimensional across much of the tunnel span, though it extends further upstream near the corners (corresponding to a less severe pressure gradient). Note that the location and size of the separation correlates well with the separated region identified from oil-flow visualisation.

The pressure along the tunnel centre span (figure 4b) displays a sharp pressure rise corresponding to the separation shock. Downstream of the separation shock, instead of a plateau underneath the separation bubble followed by a second pressure rise, the measurements show instead a smeared, more gradual increase in pressure.

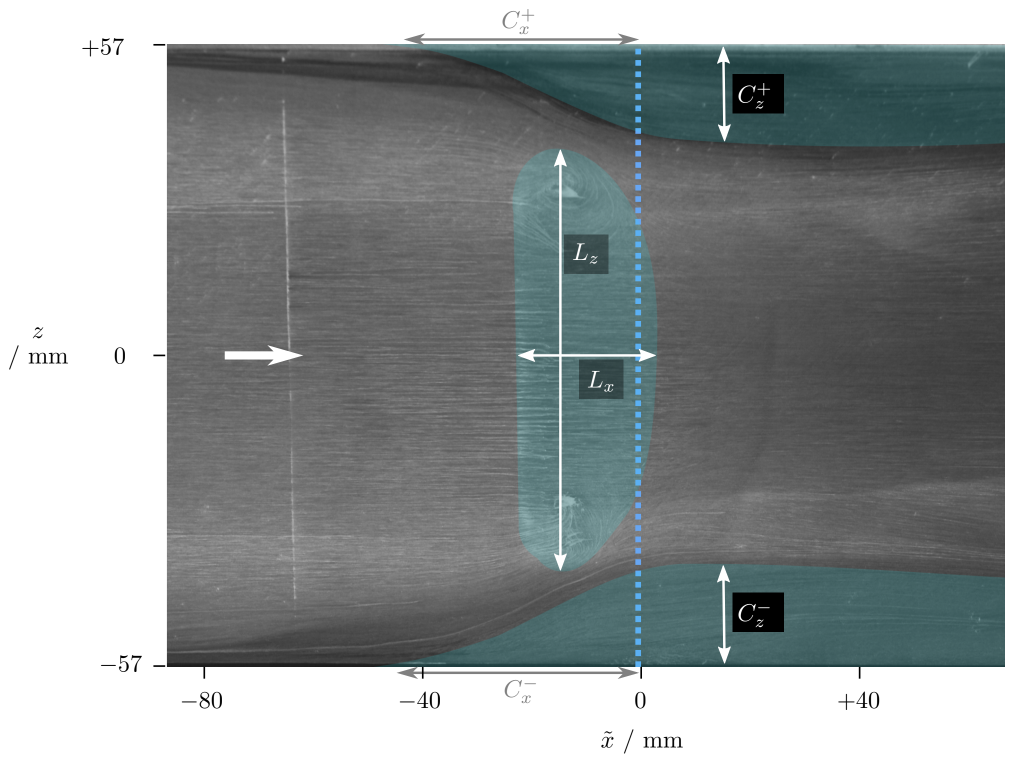

Figure 9. Oil-flow image of the separated flowfield on the tunnel floor with setup A. The regions of separation are highlighted in blue and the inviscid shock reflection line is marked by a dotted line. The labeled separation parameters are detailed in table 2.

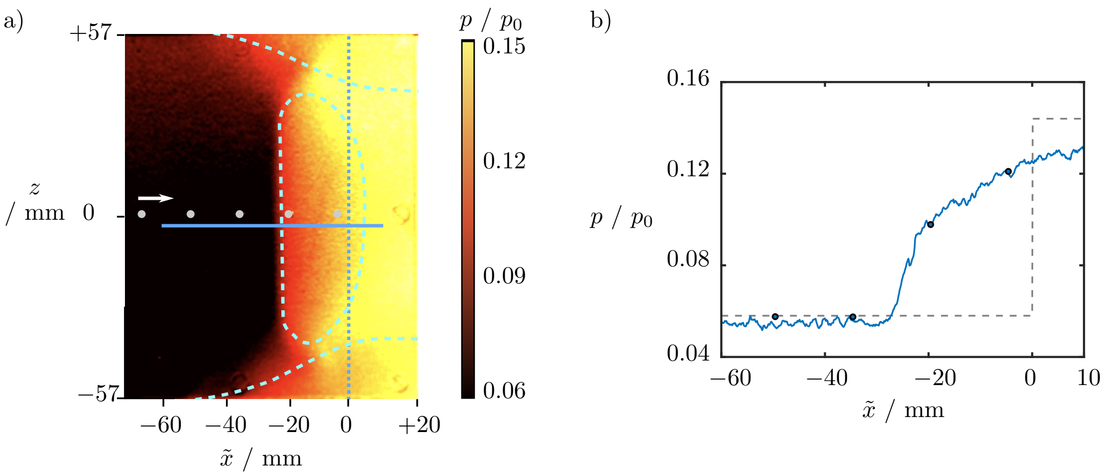

Figure 10. PSP measurements on the tunnel floor for setup A: a) the static pressure distribution over the entire floor, (dotted line shows the inviscid interaction location, dashed line shows separation regions extracted from oil flow and dots mark the locations of pressure taps); b) pressure measurements at $z = -1$ mm, including a comparison with pressure taps (dashed line shows the inviscid pressure distribution).

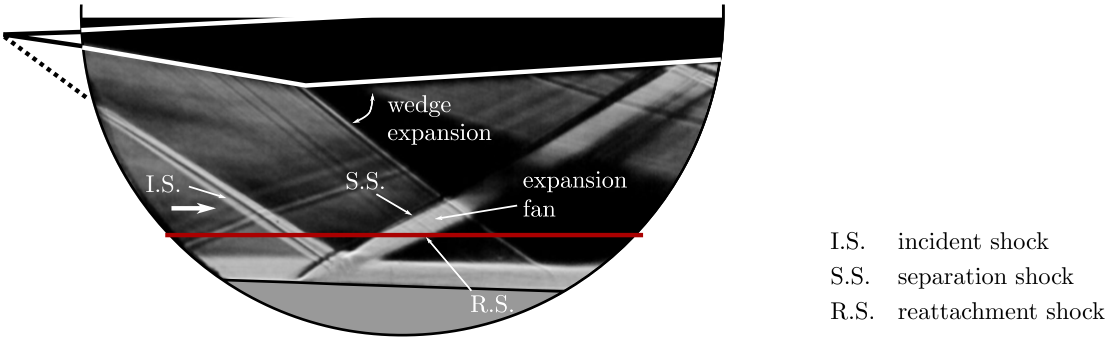

Figure 11. Schlieren image of the oblique shock–boundary-layer interaction for setup B. The red line denotes the LDV traverse location for figure 12.

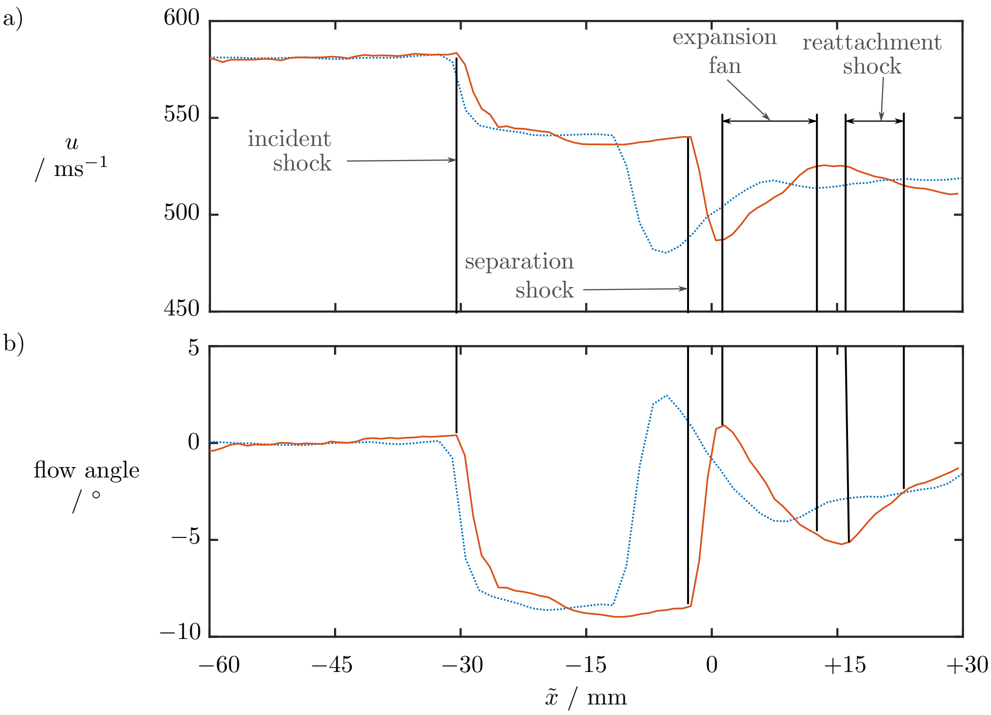

Figure 12. Streamwise LDV traverse at $y = 15$ mm and $z = 0$ mm, for setup B. The figure shows a) streamwise velocity u, and b) the local flow angle, measured upwards from horizontal. The dotted blue line corresponds to the equivalent measurements from setup A.

Setup B

A schlieren image of the oblique shock reflection with setup B is shown in figure 11. This wave pattern, similar to that presented in figure 7, is typical of a separated oblique SBLI. The incident shock, separation shock, expansion fan and reattachment shock are all evident in the schlieren image, at approximately the same angles and relative positions as for setup A. The only obvious difference between the two schlieren images is the absolute location of the interaction. This is due to the 3 mm difference in vertical position of the wedge between the two setups.

A streamwise LDV traverse 15 mm from the tunnel floor is presented in figure 12, in comprarison with figure 8. The streamwise velocity u shows a profile in accordance with the waves captured in the figure 11. The velocity drops as it passes through the incident shock at $\tilde{x} = -30$ mm, and deflects by

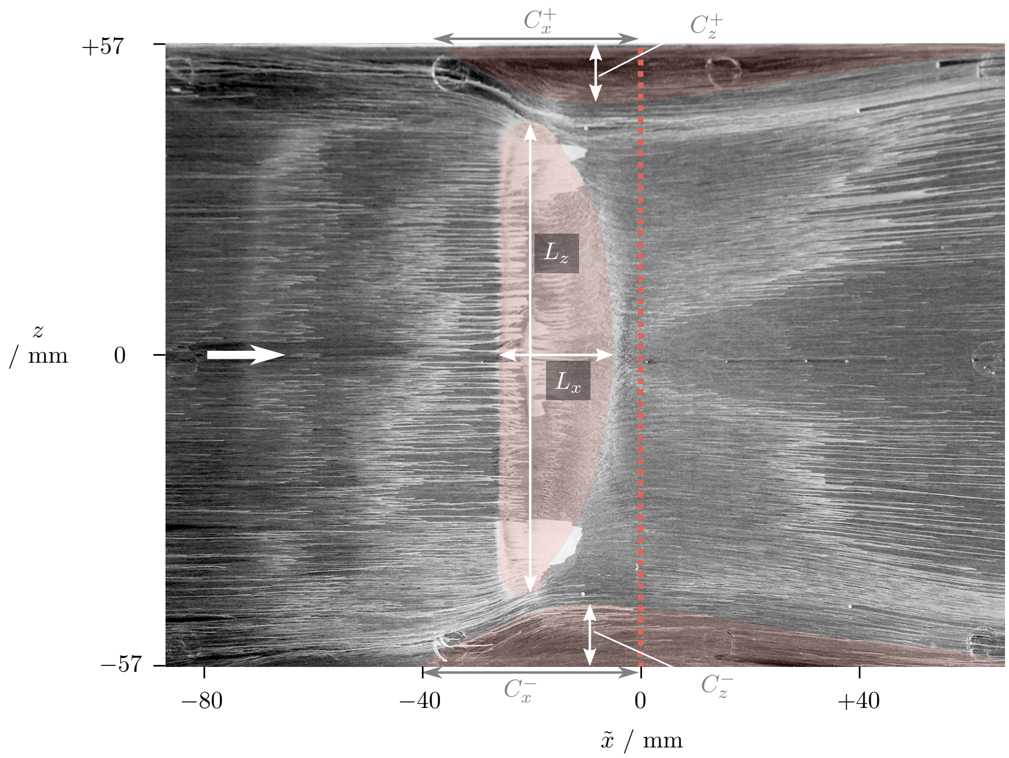

Figure 13. Oil-flow image of the separated flowfield on the tunnel floor with setup B. The regions of separation are highlighted in blue and the inviscid shock reflection line is marked by a dotted line. The labeled separation parameters are detailed in table 2.

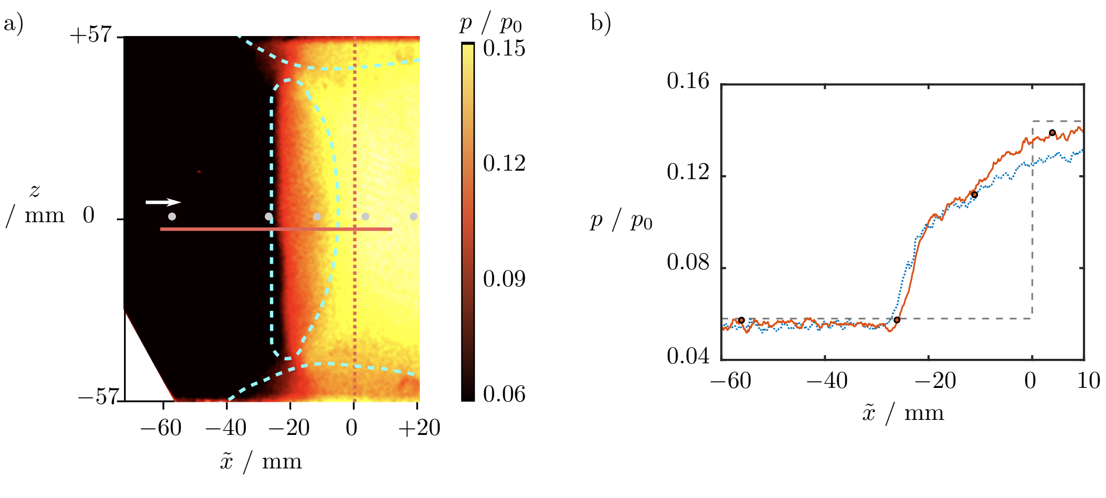

Figure 14. PSP measurements on the tunnel floor for setup B: a) the static pressure distribution over the entire floor, (dotted line shows the inviscid interaction location, dashed line shows separation regions extracted from oil flow and dots mark the locations of pressure taps); b) pressure measurements at $z = -1$ mm, including a comparison with pressure taps (dashed line shows the inviscid pressure distribution and blue dotted line is the equivalent measurement from setup A).

Setup	L_x / mm	L_z / mm	C_x^+ / mm	C_z^+ / mm	C_x^- / mm	C_z^- / mm
A	25.2	77.0	43.1	17.3	44.4	17.9
B	20.7	85.5	37.8	10.5	39.8	11.2

Table 2. Separation parameters determined from oil-flow visualisation presented in figures 9 and 13.

$7.6 \pm 1.1°$, in accordance with the intended flow deflection of 8°. As with setup A, the two deceleration regions corresponding to the separation shock and reattachment shock, respectively, bound the acceleration due to the expansion fan.

Figure 13 shows that surface oil-flow visualisation on the tunnel floor is very similar in topology to that from setup A. There is a region of central separation, which extends 20.7 mm in the streamwise direction and covers 75% of the tunnel span. Separated by a narrow channel of attached flow are regions of corner separation on each side. These begin 16.1 mm and 14.1 mm further upstream than the central separation and cover 9.8% and 9.2% of the tunnel span, in the negative-z and positive-z corners, respectively.

On closer comparison with the oil-flow image from figure 9, there are some notable differences. Setup B experiences a corner separation which starts further downstream and covers a smaller spanwise extent than setup A. In addition, the complex, three-dimensional corner separation of setup B has a footprint on the tunnel floor somewhat akin to a closed separation bubble with reattachment. The central separation is also both wider and shorter than the counterpart from setup A.

The pressure distribution over the tunnel floor is presented in figure 14. As for setup A, the separation region correlates well with that identified from the oil-flow image. The pressure is uniform upstream of the interaction, followed by a rapid pressure rise across the SBLI. This is even more two-dimensional than for setup A. The pressure rise still extends further upstream in the corners, but less so than for the other setup.

Analysis of flow fields

An extensive description of a very similar separated flowfield has been provided by Xiang [5]. The flow topology exhibits departures from a two-dimensional separation due to corner effects. The corner boundary layer, with its low momentum, separates further upstream. The displacement effect of this corner separation produces a series of compression and expansion waves which propagate into the flow. These waves, evident in the surface pressure distribution, modify the pressure gradient imposed by the incident shock. In particular, where these waves are ahead of the interaction, they reduce the overall adverse pressure gradient, and so prevent or reduce separation. This explains the narrow channels of attached flow that remain between the

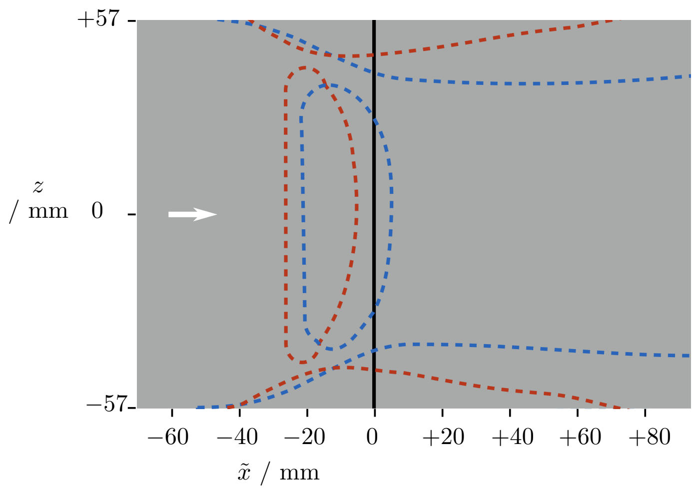

Figure 15. Comparison of floor separation topology between setup A (blue) and setup B (red).

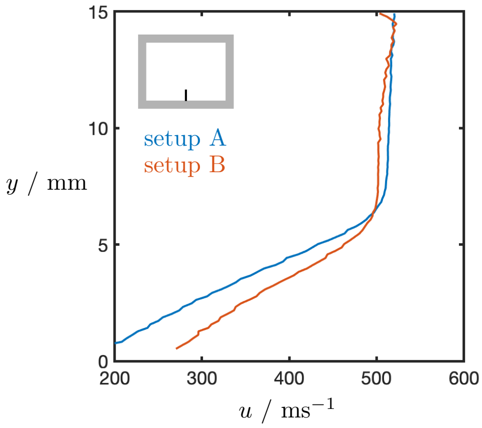

Figure 16. Comparison of the floor boundary-layer profile on the centre span at $\tilde{x} = 20$ mm for setup A (blue) and setup B (red).

central separation and corner separations.

The focus of this study is, however, the comparison between the two setups, A and B, in order to determine the influence of corner boundary-layer momentum on the characteristics of the separated flowfield. The differences in behaviour are summarised by the comparison of separated regions, determined by oil flow and shown in figure 15. Setup B, which has a higher corner momentum, is seen to exhibit the onset of corner separation further downstream than setup A. Moreover, the corner separation is less wide than for setup A. This behaviour is in agreement with an intuitive understanding that a corner boundary layer with higher momentum would be more resistant to separation, and exhibit a less severe corner separation.

The differences in corner separation affect the rest of the separated flowfield through the waves generated due to the displacement effect. In general, these take the form of compression waves followed by expansion waves. However, the expansion waves in these two setups occur too far downstream to have an effect on the main interaction itself. Therefore, we need only consider the compression waves for now.

The spanwise extent of the central separation is larger for setup A than in setup B – this is a consequence of the differences in corner separation. In setup A, the corner separation is wider and starts further upstream than setup B. Therefore the corner compression waves are ahead of the main interaction for a greater proportion of the span. This leads to a less wide central separation for setup A, since a larger fraction of the span is occupied by either the corner separation or the attached channels where the pressure rise is smeared by the corner waves.

The differences in streamwise extent of the central separation can also be explained by the corner waves. In setup A, the corner separation is large, and so the compression waves generated are relatively strong. Therefore, the central separation sees a larger overall pressure rise, and is extended in the streamwise direction. On the other hand, setup B has a smaller corner separation and so the associated compression waves are weaker. The increase in overall pressure rise seen on the tunnel centreline is smaller, resulting in a shorter central separation.

The differences in flow field between the two setups might appear to be relatively minor when considering the footprint of the interaction on the tunnel floor. However, the severity of the central separation is reflected in the state of the floor boundary layer downstream of the interaction, and this indeed exhibits more pronounced differences. Figure 16 shows the centre-span floor boundary-layer profile 20 mm (i.e. three incoming boundary-layer thicknesses) downstream of the inviscid interaction location. The boundary layer is significantly more full in setup B than setup A, which suggests that it has recovered more quickly post-interaction. This provides further evidence that, for the case with a higher-momentum corner flow, the central separation has a milder impact on the incoming flow.

V. Conclusions

This paper presents an experimental investigation designed to determine how the flow in a supersonic channels corner boundary layer affects shock-induced separation, in the corner and elsewhere. This is performed using two different nozzle setups which produce the same core flow and floor boundary layer. However, nozzle-induced secondary flows in the sidewall boundary layers cause the sidewall-floor corner regions to be quite different for the two setups, with the corner boundary layer much thicker in one than the other. An oblique shock, corresponding to 8° flow deflection, is generated in the Mach 2.5 flow – this impinges on the floor, and the response of the boundary layers is studied.

These tests show that the setup with healthier corner boundary layers is more resistant to the adverse pressure gradient of the oblique shock, since it exhibits a corner separation which starts further downstream and covers a smaller spanwise extent than in the configuration with a thick corner boundary layer. The differences in corner separation between the two setups also influence the central separated region of the floor boundary layer. The high-momentum corner flow setup, with a small corner separation, generates only weak compression waves due to the associated displacement effect. There is therefore a smaller additional adverse pressure gradient on top of that imposed by the oblique shock, resulting in a wider (i.e. more two-dimensional) and shorter central separation than the other setup. The downstream floor boundary-layer profile is more full with the higher-momentum corner flow, providing further evidence for a milder central separation.

The investigation therefore contributes towards a physical framework with which to understand and interpret oblique shock-induced separation in supersonic channel flows. In doing so, it also serves to highlight the significant influence that nozzle geomety can have on wind tunnel experiments which focus on the response of a floor boundary layer to an incident shock. It is notable that, simply by changing the nozzle geometry on an otherwise identical flow, the resulting separated flowfields are quite different.

This study provides a more complete understanding of the separated flow topology in a supersonic channel flow which encounters an oblique shock. Whilst the reliable prediction of corner boundary layers is still a topic of active investigation, it is generally understood that in applications with vertical pressure gradients (such as wind tunnels or aircraft inlets) the resulting secondary flows in the sidewall boundary layers play a major role in influencing the flow structure in the corners [12]. This investigation shows how the flow structure, and thus momentum, in the corner boundary layer, influences the separation properties in this region. The resultant effects on the rest of the flowfield can then be understood in the context of the established corner wave mechanism [5].

It is worth also noting that two-dimensional nozzle geometries (which influence the corner boundary layers) are ubiquitous in supersonic wind tunnels with rectangular cross-section. Therefore the interpretation of associated separation experiments, and especially comparison between different facilities, must account for the installed nozzle geometries. Furthermore, the comparison with simulations or validation of computational codes require a knowledge of the nozzle geometry applied.

Acknowledgments

This material is based upon work supported by the US Air Force Office of Scientific Research under award number FA9550–16–1–0430. The authors would like to thank David Martin, Sam Flint, Anthony Luckett and Ciaran Costello for operating the blowdown wind tunnel. The wind tunnel is part of the UK National Wind Tunnel Facility (NWTF) and their support is gratefully acknowledged.

References

[1] J. Benek. Corner flows: motivation & objectives. Comments made at the *10th Annual Shock Wave/Boundary Layer Interaction (SWBLI) Technical Interchange Meeting*, 2017.

[2] R.M. Chriss, W.R. Hingst, A.J. Strazisar, and T.G. Keith. An LDA investigation of three-dimensional normal shock wave boundary-layer interactions. In *Proceedings of Transonic Symposium: Theory, Application and Experiment*, volume 1, pages 741–764, 1989.

[3] P.J. Bruce, H. Babinsky, B. Tartinville, and C. Hirsch. Corner effect and asymmetry in transonic channel flows. *AIAA Journal*, 49(11):2382–2392, 2011.

[4] J. Benek, C. Suchyta, and H. Babinsky. The effect of tunnel size on incident shock boundary layer interaction experiments. In *51st AIAA Aerospace Sciences Meeting including the New Horizons Forum and Aerospace Exposition*, 2013-0862.

[5] X. Xiang and H Babinsky. Corner effects for oblique shock wave/turbulent boundary layer interactions in rectangular channels. *Journal of Fluid Mechanics*, 862:1060–1083, 2019.

[6] X. Xiang and H. Babinsky. An experimental study of corner flow control applied to an oblique shock-wave/boundary-layer interaction. In *56th AIAA Aerospace Sciences Meeting*, 2018-1532.

[7] N. Titchener and H. Babinsky. Shock wave/boundary-layer interaction control using a combination of vortex generators and bleed. *AIAA Journal*, 51(5):1221–1233, 2013.

[8] H. Babinsky, J. Oorebeek, and T. Cottingham. Corner effects in reflecting oblique shock-wave/boundary-layer interactions. In *51st AIAA Aerospace Sciences Meeting including the New Horizons Forum and Aerospace Exposition*, 2013-0859.

[9] F.B. Gessner, S.D. Ferguson, and C.H. Lo. Experiments on supersonic turbulent flow development in a square duct. *AIAA Journal*, 25(5):690–697, 1987.

[10] D.O. Davis and F.B. Gessner. Further experiments on supersonic turbulent flow development in a square duct. *AIAA Journal*, 27(8):1023–1030, 1989.

[11] D.O. Davis, F.B. Gessner, and G.D. Kerlick. Experimental and numerical investigation of supersonic turbulent flow through a square duct. *AIAA Journal*, 24(9), 1986.

[12] K. Sabnis, D. Galbraith, H. Babinsky, and J. Benek. The influence of nozzle geometry on corner flows in supersonic wind tunnels. In *57th AIAA Aerospace Sciences Meeting*, 2019-1650.

[13] L.C. Squire. The motion of a thin oil sheet under the steady boundary layer on a body. *Journal of Fluid Mechanics*, 11(2):161–179, 1961.

[14] J.W. Gregory, K. Asai, M. Kameda, T. Liu, and J.P. Sullivan. A review of pressure-sensitive paint for high-speed and unsteady aerodynamics. *Proceedings of the Institution of Mechanical Engineers, Part G: Journal of Aerospace Engineering*, 222(2):249–290, 2008.

[15] M. Sajben. Uncertainty estimates for pressure sensitive paint measurements. *AIAA Journal*, 31(11):2105–2110, 1993.

[16] S.P. Colliss, H. Babinsky, K. Nübler, and T. Lutz. Vortical structures on three-dimensional shock control bumps. *AIAA Journal*, pages 2338–2350, 2016.

[17] C.C. Sun and M.E. Childs. A modified wall wake velocity profile for turbulent compressible boundary layers. *Journal of Aircraft*, 10(6):381–383, 1973.

[18] A.J. Musker. Explicit expression for the smooth wall velocity distribution in a turbulent boundary layer. *AIAA Journal*, 17(6):655–657, 1979.

[19] N. Titchener, S. Colliss, and H. Babinsky. On the calculation of boundary-layer parameters from discrete data. *Experiments in Fluids*, 56(8):159, 2015.